Axisymmetric time-dependent flow in the Taylor-Couette system

U. Gerdts, J. von Stamm,* Th. Buzug,† and G. Pfister
Institut für Angewandte Physik, Universität Kiel, 24098 Kiel, Germany
(Received 9 August 1993; revised manuscript received 15 November 1993)

The experimental results reported in this paper concern a very slow time-periodic axisymmetric oscillation of the entire Taylor vortex system with an azimuthal wave number $m=0$ appearing as a secondary or higher time-dependent instability only. Therefore it is qualitatively different from other nonstationary states such as the wavy Taylor vortex flow or modulated wavy vortex flow. It is shown that this flow state is caused by the coupling strength of the phases of the underlying wavy flow modes. The observed oscillation frequencies range from 2×10^{-2} to 3×10^{-5} times the inner cylinder's angular velocity. Thus, we call this flow the very low frequency (VLF) mode. Up to now there has been no satisfactory theory which can explain the appearance of this mode.

PACS number(s): 47.20.−k, 05.45.+b

I. INTRODUCTION

The Taylor-Couette flow, which is one of the classical pattern-forming systems in hydrodynamics, consists of a viscous fluid between two concentric cylinders with the inner one rotating, the outer cylinder and end plates being held at rest. Increasing the inner cylinder's angular velocity Ω_i, which is proportional to the Reynolds number Re, the flow undergoes a series of transitions (the "main sequence") which are characterized by changes in the symmetry group that leave the flow invariant [1]. When the Reynolds number is very small, the Couette flow for infinite cylinders is a good approximation of the flow for long finite cylinders, except near the end plates. However, when Re is increased to a quasicritical range near Re_c, the flow becomes centrifugally unstable and changes to a regular cellular vortex structure in which ring vortices alternating in flow direction enclose the axis of rotation. The flow remains stationary and the vortex structure is axisymmetric and periodic in axial direction with wavelength λ. This flow is called Taylor vortex flow (TVF) after Taylor [2], who first described it theoretically (for infinite cylinders) and experimentally. The lower stability limit for TVF in (λ,Re)-parameter space can be explained by the Eckhaus mechanism [3,4]. The Navier-Stokes equations linearized around Taylor vortex flow are autonomous in the azimuthal coordinate Θ and time t, so generically any mode which breaks these symmetries will have the mathematical form of a rotating wave. In this time-dependent flow regime (which we refer to as wavy Taylor vortex flow or WVF) the motion becomes time independent when observed in a corotating frame [5].

Except for the experimental observation of solitary waves propagating in axial direction in a counter-rotating system [6] until now, to our knowledge, exclusively time-periodic flow modes with an azimuthal wave number $m\geq1$ (breaking the azimuthal symmetry) have been found in the Taylor-Couette experiment. The axisymmetric time-dependent flow, observed by us, exhibits an azimuthal wave number $m=0$ and thus breaks the axial, but not the azimuthal, symmetry of the cylindrical flow system. As a step towards understanding the appearance of turbulent flows, it is important to understand what determines the limit of stability for this preturbulent flow regime. Therefore in the last section of this paper we present a discussion of a mechanism for the onset of this flow mode. In Sec. II we introduce the experimental setup. In the third section we give a short overview of the time-periodic flow states found in the Taylor-Couette system up to now (which appear as the underlying flow states of the very low frequency mode in our experiment). In the fourth section, which is divided into two subsections, we present (i) experimental results of the different types of underlying wavy flow modes and (ii) the investigation of the very low frequency (VLF) mode. In the fifth section we give experimental evidence for a mechanism that causes the appearance of the VLF mode, which is discussed in the final section.

II. EXPERIMENTAL SETUP

The flow of interest is bounded by two high-precision coaxial cylinders. The rotating inner cylinder of the Taylor-Couette experiment is machined from stainless steel having a radius of $r_i=12.5$ mm. The stationary outer cylinder is made of optical polished glass with a radius of $r_0=25.0$ mm giving a radius ratio of $\eta=0.5$. The accuracy of the radii is better than 0.01 mm over the entire length of 640 mm. We measured an eccentricity of the cylinders of $\varepsilon\leq0.005$ mm and therefore the power spectrum of the local velocity distribution is noticeable by the absence of Ω_i at any location in the fluid.

The top and bottom plates are at rest. The length of the gap can be varied continuously by moving the metal collar which provides the top surface of the flow domain.

*Electronic address: pan15@rz.uni-kiel.d400.de
†Present address: Forschungsanstalt der Bundeswehr für Wasserschall- und Geophysik, Klausdorfer Weg 2-24, 24148 Kiel, Germany.

The aspect ratio $\Gamma = L/d$ used as a geometric control parameter is defined as the ratio of gap length L to gap width $d = r_0 - r_i$. As a working fluid we use silicon oil with different viscosities ν depending on the flow situation. The Reynolds number is then defined as $\mathrm{Re} = (\Omega_i r_i d)/\nu$, where ν is the kinematic viscosity. The temperature of the fluid is held constant to within 0.01 K by circulating thermostatically controlled oil through a surrounding square box. A phase-locked-loop (PLL) circuit controls the speed of the inner cylinder with an accuracy of better than one part in 10^{-4} per revolution and one part in 10^{-7} in the long-term average. The uncertainty of the absolute value of the Reynolds number is smaller than 1%.

To ensure that the measured phenomena are not artificial and not due to inaccuracies of the experimental equipment, we used three different experimental setups. All effects we focus on could be found independently in each device. The local velocity is measured by a laser-Doppler velocimeter (LDV) and recorded by a PLL analog tracker.

III. THE UNDERLYING FLOW STATES

Using Floquet theory one defines a rotating wave as a solution for the Navier-Stokes equations with the symmetry

$$Q_W(r,\Theta+\delta\Theta,z,t) = Q_W(r,\Theta,z,t-\delta\Theta/c_1) , \tag{1}$$

where Q_W is an arbitrary scalar flow quantity in the rotating wave state and c_1 the dimensionless wave speed. The flow is m_1-fold symmetric,

$$\Theta \rightarrow \Theta + \frac{2\pi}{m_1} , \tag{2}$$

where m_1 is the azimuthal wave number ($m \geq 1$). The Θ and t coordinates are coupled and periodic, so the solution has the general form

$$Q_W(r,\Theta,z,t) = \sum_{j=-\infty}^{\infty} b_j(r,z) e^{ijm_1(\Theta - c_1 t)} . \tag{3}$$

In a power spectrum of an experimental time series there is a set of equally spaced peaks at multiples of $m_1 c_1$, thus one defines $\omega_1 = m_1 c_1$ as the fundamental frequency of the rotating wave [7]. The flow will be time independent if observed in a frame rotating with an angular speed $c = c_1$. Defining the new variable

$$\hat{\Theta} = \Theta - c_1 t \tag{4}$$

the flow $Q_W(r,\hat{\Theta},z)$ becomes steady. The wavelength dependence of the onset of WVF and some types of wavy flow modes which arise have been investigated by Jones [8], Pfister, Lorenzen, and Mullin [9], Mullin [10], and King and Swinney [11].

Following the main sequence the primary time-periodic rotating wave bifurcates to a doubly periodic flow regime (which we refer to as modulated wavy vortex flow or MWVF). Assuming that there is no change in the axial structure of the solution, the flow goes through a supercritical Hopf bifurcation to modulated waves and taking into account that the fully nonlinear solution for the MWVF must contain all the modes that might be generated as products of the eigenmode with itself or the rotating wave, the MWVF solutions can be written as a spectral sum of these products, having the general form

$$Q_M(r,\hat{\Theta},z,t) = \sum_{j=-\infty}^{\infty} \sum_{k=-\infty}^{\infty} a_{jk}(r,z) e^{ijm_1\hat{\Theta}} e^{ik(m_2\hat{\Theta} - \omega_M t)} \tag{5}$$

in the c_1 frame. ω_M is defined as the modulation frequency observed in the corotating frame. The wave number m_2 need not equal m_1, so the azimuthal symmetry of the flow may be changed by the bifurcation [7]. Such flows have been discovered by Gorman and Swinney (GS mode) [12] and Zhang and Swinney (ZS mode) [13], occurring as preturbulent flow regimes, and by King and Swinney (KS mode), who found a different kind of modulated flow which occurs as a result of the competition of at least two WVF modes (with different azimuthal wave numbers) for dominance [11]. Coughlin and Marcus have performed numerical simulations of the stability of GS and ZS modes, showing that several branches of quasiperiodic solutions exist, and not all of them occur as direct bifurcations from rotating waves as the main sequence suggests [14].

IV. RESULTS

A. The underlying wavy Taylor vortex flows

In experiments one observes physically different modes that have the symmetry of Eqs. (1) and (2). The special physical type of these rotating waves (which we refer to as the time-dependent flow modes), each of them undergoing a supercritical Hopf bifurcation, depends on geometrical boundary conditions. Figure 1 shows the stability diagram for the normal four- to 16-vortex flow. (The occurrence of the normal modes is caused by the centrifugal force falling off towards the fixed ends of the cylinders so there is inward-directed flow at the stationary end plates.) As a geometrical control parameter the aspect ratio Γ is varied. By the number of vortices and the size of Γ the length of the vortices ($\lambda/2 = \Gamma/N$) can be adjusted.

It can be seen from the diagram in Fig. 1 that the range of stationary vortices is largest for a wavelength having the same size as the gap width d ($\Gamma/N \approx 1$) independent of the aspect ratio Γ. The stability line (a) shows the transition to the *small-jet* mode. This mode is an oscillation of the outward flow while the inward flow is almost stationary. Adjacent outward flows oscillate in antiphase [8,15]. It is remarkable that this line in the normalized stability diagram is the same for all small-jet modes occurring in six- to 16-vortex flow. That means that the onset of this mode is independent of the number N of vortices of the underlying flow pattern. For increasing Reynolds numbers line (a) goes towards $\Gamma/N = 0.96$. Line (b) displays the stability for the *antijet* mode, an oscillation having the main amplitude in the inward flow [16,17]. The stability lines (c) for the *wavy* mode [18], an axial oscillation of the entire vortex occurring in eight- to 16-

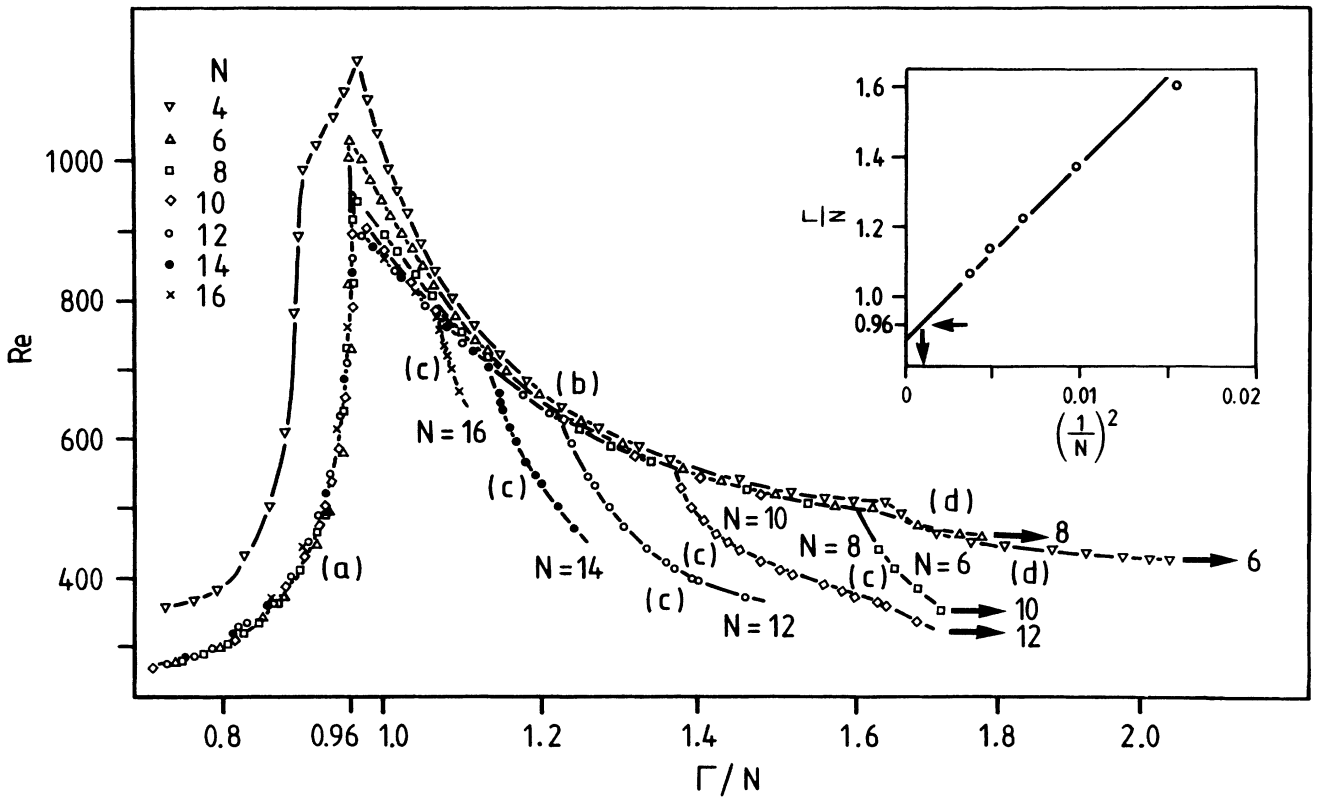

FIG. 1. Normalized stability diagram for the onset of time dependence in a Taylor-Couette system with $\eta=0.5$ for the normal four- to 16-vortex flow.

vortex flow, which can be identified with the classical narrow-gap wavy mode [8], and the stability lines (d) for the *core* modes, which are oscillations of the vortex core occurring only in the four- and six-vortex flow as a primary time-dependent mode, are located in the large-λ range.

The antijet mode occurs as three subtypes exhibiting different spatial distributions of their amplitudes [17]. The space dependence of the order parameter in Taylor-Couette flow can be satisfactorily described with the time- and space-dependent Ginzburg-Landau equation, which was shown by Pfister and Rehberg [19]. For brevity we will call the first subtype the bell-shaped mode, having its largest amplitude in the middle of the cylinder length, "the bell mode," and the second subtype, having end-induced amplitudes, the "end modes." The bell mode occurs for smaller wavelengths ($0.96<\Gamma/N<1.15$) in the antijet regime, whereas the end mode occurs in regions of very extended vortex length ($1.15<\Gamma/N<1.7$). Both subtypes have a symmetrical amplitude distribution relative to the midplane of the apparatus ($z=L/2$). The third subtype which breaks this symmetry occurs at higher Reynolds numbers and will be discussed elsewhere.

The inset in Fig. 1 illustrates the dependence of the transition point between antijet and wavy mode as a first oscillatory instability as a function of increasing vortex numbers. These transition points are plotted versus the reciprocal value of the squared vortex number $(1/N)^2$ showing a linear dependence. The intersection point of this straight line with $\Gamma/N=0.96$ gives a value of approximately $(1/N)^2=1.1\times10^{-3}$ which yields $N=30$. This reveals that for $N>30$ no antijet mode can be observed as a first time-dependent mode any more. This agrees with the L^2 dependence of the shift of the onset of the wavy flow modes found experimentally in [19] and by analyzing the Ginzburg-Landau equations.

One further oscillatory mode occurs in the Taylor-Couette system for $\eta=0.5$ appearing for wavelengths $\lambda<2$. It is a second mode showing oscillations of the outward flow, the *large-jet* mode, which can be identified by a very large amplitude and, in contrast to the small-jet mode, adjacent outward flows oscillate in phase [15]. Due to the fact that (i) adjacent outward flows of the small-jet mode oscillate in antiphase, adjacent outward flows of the large-jet mode oscillate in phase, (ii) the large-jet mode occurs for Reynolds numbers slightly larger than those for the occurrence of the small-jet mode, and (iii) the wave speed in times of the inner cylinder speed of the large-jet mode is a little larger than for the small-jet mode, we conjecture that small- and large-jet modes can be identified with the subharmonic and the harmonic jet mode, respectively, found by Jones numerically [8]. Table I gives an overview of the five different time-dependent modes for a cylinder with radius ratio $\eta=0.5$. In this table we used the notation of Demay and Iooss [20] for the classification of the symmetry invariances. Table I includes a sixth time-periodic flow mode, the VLF mode, which is a very slow time-periodic axisymmetric shift of the entire vortex system

TABLE I. Six time-dependent modes occurring in the Taylor-Couette system with $\eta=0.5$.

Label	Characteristics	Subtype(s)	Wave number $\eta=0.5$	Wave speed (in times of the inner cylinder speed) $\eta=0.5$	Reflection (about the outflow boundary)	Axial translation
Small jet	wavy outflow boundary	bell mode	$m=1$	0.46–0.52	−	−
Large jet	wavy outflow boundary	bell mode	$m=1$	0.54–0.60	−	+
		bell mode		0.90–0.93		
		end mode	$m=5$	0.87–0.89		
Antijet	wavy inflow boundary	asymmetr.		0.91–0.93	+	−
		bell mode	$m=4$	0.70–0.76		
		end mode				
Core	wavy core flow	end mode	$m=5$	1.10–1.12	0	0
Wavy	wavy vortex flow	bell mode	$m=1$	0.09–0.125	−	+
VLF	axial symmetric long-wave modulation of the entire vortex system	bell mode	$m=0$	$<2\times10^{-2}$	0	0

with an azimuthal wave number $m=0$. Due to the fact that the VLF mode does not have the mathematical form of a rotating wave [Eq. (3)], it appears only as a secondary or higher instability.

B. The VLF mode

The VLF mode was observed for flow systems with vortex numbers $N=4$, 8, 10, 20, 30, and 40 in three different experimental setups with three different oil viscosities. For the eight- and ten-vortex flow it was investigated systematically.

All experimental observations support the conjecture that there is a causal connection between the appearance of the VLF mode and the presence of one of the ($m\neq0$) modes, because the VLF mode occurs as a secondary time-dependent mode only. The VLF mode appears in the entire measured range as shown in Fig. 2 for the ten-vortex flow. The Reynolds number is plotted versus aspect ratio Γ normalized to the number of vortices N. The onset of the VLF mode is marked with the lines including the triangles whereas all other measured stability lines in this diagram are marked with circles. The lines denoting the transitions to the first oscillatory instability are the same as in Fig. 1 for the ten-vortex flow (marked with the diamonds in that figure). On the left-hand side one finds the small-jet mode, on the right-hand side the wavy mode, and in midrange the antijet mode, which is divided into two subtypes, the bell mode (marked with B) and the end mode (marked with E), respectively. "$N\rightarrow8$" denotes the transition to the eight-vortex flow.

The VLF mode shows very large characteristic periods compared to the other time-dependent modes apparent from Fig. 3, which shows three different time series recorded for different aspect ratios. In these plots the axial displacement Δz of the vortex system in the middle of the cylinder ($z=L/2$) is recorded versus time t. The time series are filtered with a low-pass Bessel filter of fourth order having a cutoff frequency at 0.2 Hz to make the structure of the VLF oscillation visible, because otherwise it would be partially hidden by the underlying wavy flow mode. The measured oscillation frequency ranges from 2×10^{-2} in Fig. 3(c) to 3×10^{-5} times of the inner cylinder's angular velocity in Fig. 3(a). Furthermore, the VLF mode shows quite different dependence of amplitude A and eigenfrequency ω_s on Re, depending on the underlying time-dependent flows. The amplitude A is the maximum displacement Δz_{max} from its average value. In one example it occurs with an eigenfrequency starting from $\omega_s=0$ and a finite amplitude $A\neq0$ at onset, and in another with an eigenfrequency having a finite value $\omega_s\neq0$ and an amplitude increasing with a square-root law from the value $A=0$. The first case, which is illustrated in Fig. 4, was observed only when the underlying flow is a WVF [Eq. (3)]. The second case, which is shown in Fig. 5, corresponds to a Hopf bifurcation and was observed only when the underlying flow is a MWVF [Eq. (5)]. The examples shown in Figs. 4 and 5 are recorded for $\Gamma/N=0.8$ below and above the hatched region that marks a gap in the VLF mode domain in Fig. 2.

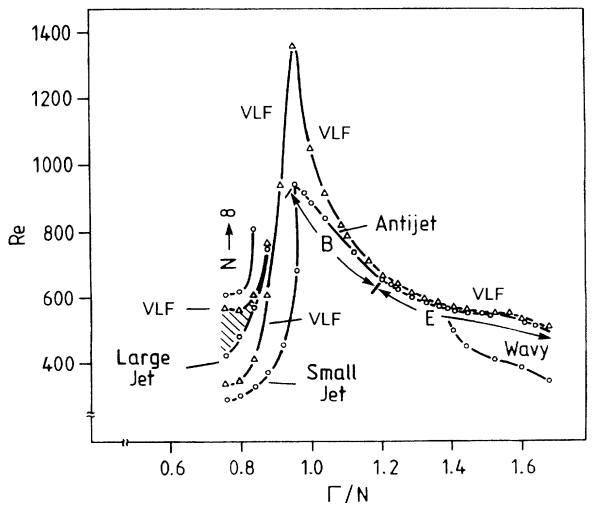

FIG. 2. Stability diagram for the onset of primary and higher oscillatory modes in the ten-vortex flow in a Taylor-Couette system with $\eta=0.5$.

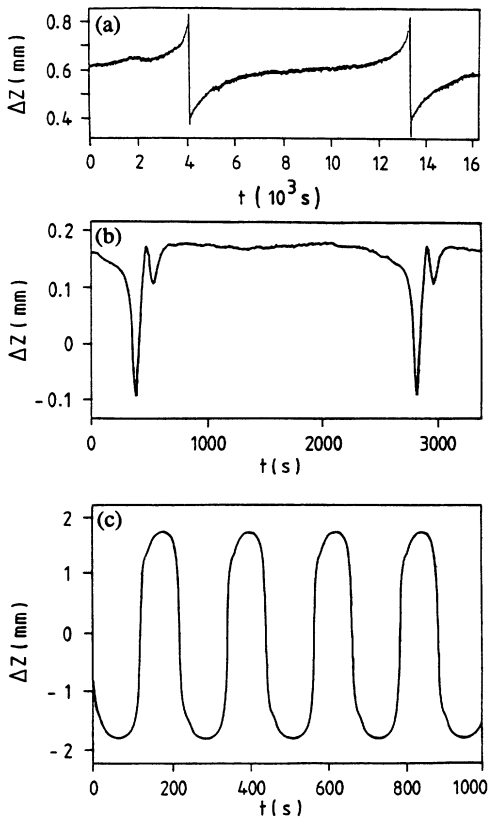

FIG. 3. Three VLF mode oscillations. (a) Slightly after its onset for $N=10$, $\Gamma/N=0.8$, Re=356.4; (b) for $N=10$, $\Gamma/N=1.18$, Re=711.3; and (c) for $N=10$, $\Gamma/N=1.04$, Re=1047.

The amplitude and form of the VLF oscillations vary with the cylinder length L. They are symmetric relative to the midplane in the antijet bell-mode regime ($0.96<\Gamma/N<1.15$) [Fig. 3(c)] and asymmetric for smaller aspect ratios when the underlying wavy flow mode is the small-jet mode ($\Gamma/N<0.96$) [Fig. 3(a)] and for larger aspect ratios in the antijet end-mode regime ($1.15<\Gamma/N$) [Fig. 3(b)].

In Fig. 6 a bifurcation diagram of the asymmetric VLF mode with the small-jet mode as an underlying wavy flow mode is shown for the ten-vortex flow for $\Gamma/N=0.84$. Here the axial displacement of the flow pattern Δz was recorded versus the Reynolds number which was scanned quasistatically from Re=325 to 530 with $\Delta\,\mathrm{Re}/\Delta t=0.025\ \mathrm{s}^{-1}$. The LDV measurement volume was placed in the midplane ($z=L/2$) of the apparatus near the inner cylinder. Thus it is suitable to characterize the deviation from the symmetric state. The bifurcation diagram was filtered with a low-pass Bessel filter of fourth order having a cutoff frequency at 0.2 Hz like the time series in Fig. 3. The bifurcation diagram shows the onset of the small-jet mode at Re≈335 via a Hopf bifurcation exhibiting a simultaneous axial symmetry-breaking bifurcation, which leads to an asymmetric distribution of the axial wave vector. In Table II the measured values for the wavelength of each vortex pair for increasing Reynolds number are given. As expected, the wavelengths of the

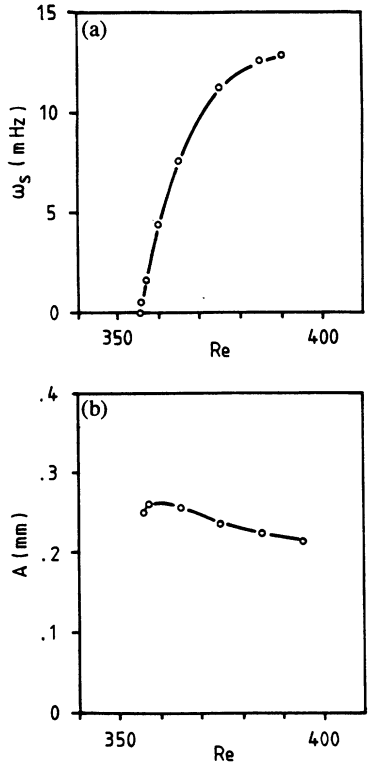

FIG. 4. (a) Eigenfrequency ω_S and (b) amplitude A of the VLF mode versus Reynolds number Re at first onset in the ten-vortex flow for $\Gamma/N=0.8$.

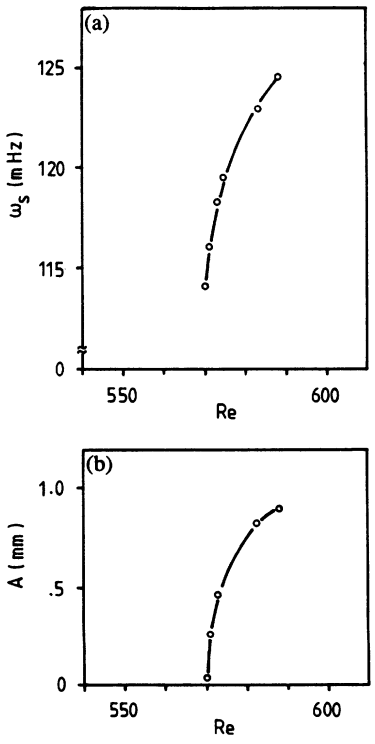

FIG. 5. (a) Eigenfrequency ω_S and (b) amplitude A of the VLF mode versus Reynolds number Re at second onset in the ten-vortex flow for $\Gamma/N=0.8$.

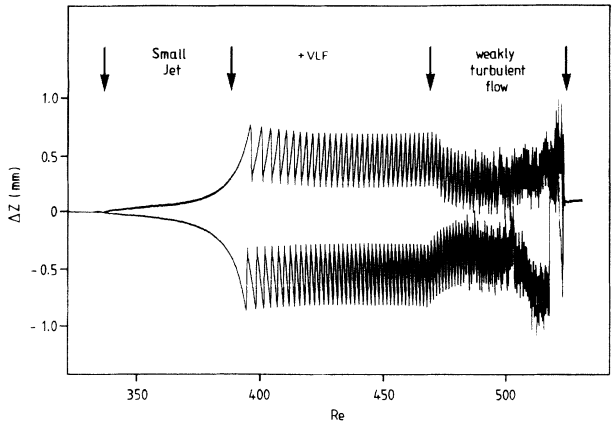

FIG. 6. Bifurcation diagram of the axial displacement of the flow pattern Δz for the ten-vortex flow for $\Gamma/N=0.84$. The Reynolds number was scanned quasistatically from $\mathrm{Re}=325$ to $\mathrm{Re}=530$ with $\Delta\,\mathrm{Re}/\Delta t=0.025\ \mathrm{s}^{-1}$.

end-vortex pairs λ_1 and λ_5 show a decay for increasing Reynolds numbers going along with an increase of the vortex pairs in between [21]. The inner vortex pair corresponding to λ_2 shows a stronger increase than the one corresponding to λ_4 leading to a distribution of the axial wave vector which breaks the axial symmetry relative to the midplane ($z=L/2$). The VLF mode oscillations appear on each branch at $\mathrm{Re}\approx 390$ with an eigenfrequency starting from very small values and a finite amplitude $A\neq 0$. Recording time series near the onset of the VLF mode starting from a slightly higher Reynolds number reveal that the eigenfrequency goes to zero at onset as shown in Fig. 4 for $\Gamma/N=0.8$. The phase relation—neighboring outward flows oscillate in antiphase—remains in the asymmetric small-jet mode till the asymmetric shifting of the vortex system reaches a certain threshold at $\mathrm{Re}\approx 390$ where the VLF mode appears. Figure 3(a) shows the oscillation of the asymmetric VLF mode in the small-jet regime slightly above its onset with an eigenfrequency of approximately $\omega_S=0.1$ mHz corresponding to a period length of about 2.5 h. The vortex system needs almost the whole period length to shift into the end position where $|\Delta z|$ reaches its maximum while the shifting back to the opposite end position needs only about 15 s. Increasing the Reynolds number the eigenfrequency ω_S grows rapidly (Fig. 6). Comparing time series shortly after onset of the VLF oscillations and slightly before the onset of the weakly turbulent flow one observes that the steep flank of the oscillation is nearly unaffected by a change in Reynolds number whereas, increasing the Reynolds number, the flat flank of the oscillation curve becomes steeper. In Fig. 3(a) the system needs about 9200 s to rise whereas slightly before the onset of the chaotic flow the rising only lasts about 50 s. The fact that the elongation back towards $\Delta z=0$ needs about 15 s independent from the Reynolds number points to a universal mechanism like a diffusive equalization of the differences in the axial wave vector. The transition to weakly turbulent flow occurs at $\mathrm{Re}\approx 465$ (Fig. 6). Due to small imperfections in the Taylor apparatus the two branches show small differences. The chaotic flow is restabilized by the onset of the large-jet mode at $\mathrm{Re}\approx 525$.

Figure 7 shows the bell-shaped amplitude distribution of the symmetric VLF mode oscillation depicted in Fig. 3(c) versus the axial position over the entire cylinder length. In Fig. 8 the wavelength distribution versus the axial position over the entire cylinder length for both end positions of the VLF oscillation and in Fig. 9 the corresponding wavelength difference $\Delta\lambda$, calculated from the differences of both curves in Fig. 8, are plotted. $\Delta\lambda$ is zero in the middle of the cylinder ($z=L/2$) having its extrema at about $z=L/4$ and $3L/4$. Neglecting the wavelength differences of the end vortices, the measured values in Fig. 9 can be fitted by a sine curve. Physically this corresponds to an inert coil spring embedded in a viscous fluid and fixed at its ends, which is elongated periodically at its middle winding.

The wave vector modulation interacts with the underlying ($m\neq 0$) modes. The small-jet and the antijet modes occurring by themselves have a fixed phase relation till the onset of the VLF mode. At the onset of the VLF mode the fixed phase relation is lost and the phase runs through multiples of 2π during a VLF period. In regions of the parameter space, where the VLF mode has disappeared and the vortex system is symmetric again, the phase relation of the underlying fast mode becomes fixed again. Such a domain can be found in Fig. 2 marked with the hatched region, where the chaotic flow is restabilized by the onset of the large-jet mode (see also the bifurcation diagram in Fig. 6).

V. THE MECHANISM FOR THE VLF MODE

The fast ($m\neq 0$) modes, which we refer to as the "fast modes," cause a change of the wavelength of the vortices

TABLE II. Wavelengths (in units of the gap width d) of a ten-vortex flow with aspect ratio $\Gamma/N=0.84$ and $\eta=0.5$ for increasing Reynolds numbers. The values correspond to one branch in Fig. 6. The measurement error amounts to ± 0.002.

Wavelength \ Reynolds number	274	338	365	384	388
λ_1/d	1.827	1.814	1.771	1.750	1.749
λ_2/d	1.581	1.590	1.615	1.634	1.637
λ_3/d	1.583	1.594	1.635	1.654	1.655
λ_4/d	1.578	1.584	1.603	1.608	1.608
λ_5/d	1.830	1.818	1.775	1.753	1.751

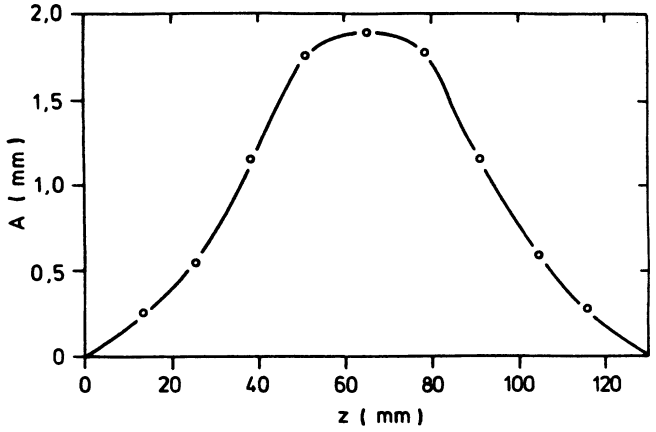

FIG. 7. Amplitude A of the VLF-mode oscillation in Fig. 3(c) versus the axial position z over the entire cylinder length.

in the flow [8,18]. Therefore there is a coupling between these modes and an axial phase diffusion [22–24]. Furthermore, the frequencies of the fast modes depend on the wavelength of the vortices [8,18,25,26]. Due to this a local disturbance of the wavelength leads to a change in the frequency. A displacement of the phases between the oscillations of neighboring vortices occurs. These phase differences are presumably the driving forces for the VLF mode.

The above considered measurements give no information whether the propagating phase causes the VLF mode or the occurrence of the VLF mode leads to a disconnection of the phases of oscillations in neighboring vortices. We give an argument for the former assumption.

Observing the antijet end mode one realizes that this mode shows a very weak phase relation between oscillations of the end vortices. This is easy to understand because the end vortices are separated by the vortices in the center of the flow having very small amplitudes. Therefore the oscillations in the end vortices have only a weak coupling of their phases. If the propagating phase causes the VLF mode, the latter has to occur nearly simultaneously with the antijet end mode. In fact this is shown in

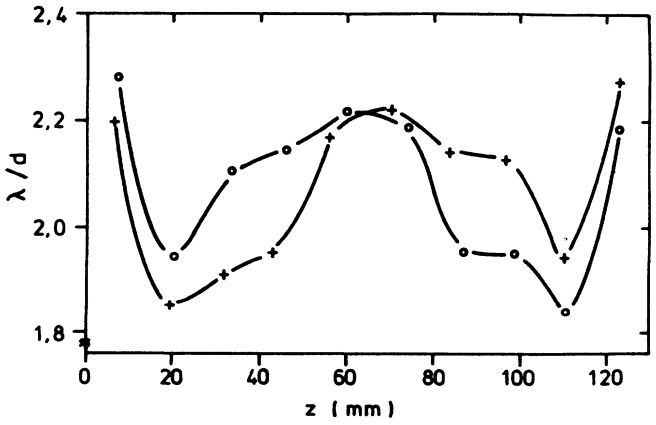

FIG. 8. Wavelength λ versus the axial position z over the entire cylinder length for both positive (0) and negative (+) end positions of the VLF-mode oscillation in Fig. 3(c).

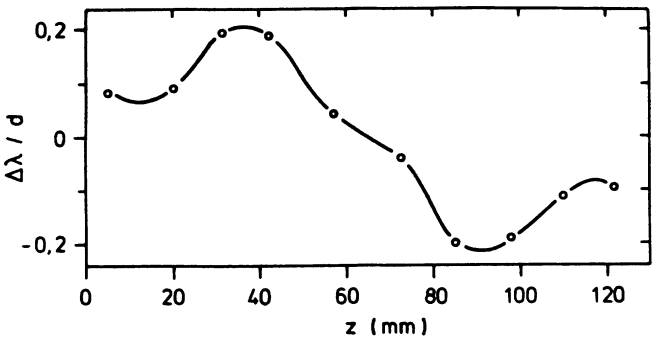

FIG. 9. Wavelength difference $\Delta\lambda$ versus the axial position z over the entire cylinder length calculated from the VLF end positions in Fig. 7.

Fig. 2 for $1.15 < \Gamma/N < 1.7$ [27].

The small-jet mode and the bell-mode subtype of the antijet mode exhibit a stronger coupling of the phases in the neighboring vortex pairs. Due to this one observes a larger Reynolds-number range between the onset of the VLF mode and these primary oscillatory modes than for parameter ranges where the core mode or the end-mode subtype of the antijet mode occur as the primary time-dependent flow mode. This is shown in Fig. 2 for $0.7 < \Gamma/N < 1.15$.

Considering the wavy mode one observes an oscillation of the entire vortex. Due to this the coupling of the phases of neighboring oscillations is very strong. Therefore, the phases do not propagate when the wavy mode is exclusively present and the onset of the VLF mode becomes impossible. In fact it has never been observed that the VLF mode occurs while the wavy mode is exclusively present. Except after the onset of a second time-dependent flow mode showing a weaker phase coupling such as the antijet or the core mode one observes the onset of the VLF mode as shown in Fig. 2 for $1.35 < \Gamma/N < 1.7$. Due to this fact, to our knowledge the VLF mode has never been observed in the classical narrow-gap experiments by Swinney and co-workers [11–13,26,28–31].

The oscillations of the core mode are separated by the inward and outward flows of the vortices, which are unaffected by the oscillation of this mode. Therefore, neighboring oscillations of the vortex cores cannot couple their phases. Due to this the VLF mode occurs simultaneously with the core mode. In fact the core mode shows no tendency to couple the oscillations of the different vortex cores. Therefore in parameter ranges where the core mode appears—opposite to regions where the antijet and the two jet modes appear—the onset of the VLF mode is not time periodic but chaotic [27]. The onset of the chaotic VLF mode will be discussed elsewhere [32].

VI. DISCUSSION

We have shown that the onset of the VLF mode is caused by the strength of the coupling of the underlying wavy flow modes. On one hand, the fast modes cause a change of the axial wavelength of the flow pattern and,

on the other hand, the frequencies of the fast modes depend on the wavelength of the vortices. Therefore we have an interaction between the wavy flow modes and the wave vector of the underlying Taylor vortex pattern [22]. Local disturbances of the wavelength lead to a change in the frequency of the wavy flow mode. These frequency differences disappear if the oscillations in neighboring vortex pairs are coupled strongly, otherwise, due to the interaction between wavy flow modes and the axial wave vector, they lead to an amplification of the local disturbance of the wavelength of the underlying Taylor vortex pattern.

Now the system tends to equalize these disturbances by an axial phase diffusion, because there is a coupling between the underlying Taylor vortex pattern and the wavy flow modes [22,23,27]. If the coupling between spatially separated oscillations of the underlying wavy flow mode becomes weak, the amplifying mechanism described above may exceed this diffusive equalization and the underlying Taylor vortex flow pattern becomes unstable at a certain threshold against an undamped oscillation of the entire vortex system in axial direction.

The conjecture that axial phase diffusion processes play an important role for the onset of the VLF mode is supported by the following argument. The axial phase shift δ of the VLF oscillations, which is defined as the displacement of different vortices normalized to the wavelength, was measured for the ten- and 30-vortex flow for several Reynolds numbers, revealing that it has a linear dependence on the axial position. To determine the phase shift of the VLF oscillations of different vortices, the radial velocity component of the flow was measured simultaneously at two different locations, a half and two wavelengths separated in axial direction [33,34]. In both flows the shift per wavelength difference is approximately 5°. That means for the ten-vortex flow that the phase shift between the two end vortices sums up to approximately 25°. This is similar to the results of the phase diffusion measurements of Wu and Andereck [see Fig. 2(b) in Ref. [23]].

In summary, careful measurements have shown that the VLF mode (a destabilization of the underlying axial wave vectors) occurs as a secondary or higher instability in the entire λ range of the control-parameter space accessible to experiments. Though the temporal behavior and the amplitude may be quite different, we think that the VLF mode displays a universal behavior in Taylor-Couette flow.

ACKNOWLEDGMENTS

We gratefully acknowledge discussions with A. Predtechensky and thank him for completion of the measurements concerning the onset of the first time-dependent modes. We also acknowledge the support of the Deutsche Forschungsgemeinschaft Grant No. Pf 210/3-2.

[1] M. Golubitsky and I. Stewart, SIAM J. Math. Anal. **17**, 249 (1986).
[2] G. I. Taylor, Philos. Trans. R. Soc. London, Ser. A **223**, 289 (1923).
[3] H. Riecke and H.-G. Paap, Phys. Rev. Lett. **33**, 547 (1986).
[4] M. A. Dominguez Lerma, G. Ahlers, D. S. Cannell, and R. Heinrichs, Physica D **23**, 202 (1986).
[5] D. Ruelle, Arch. Ration. Mech. Anal. **51**, 136 (1973).
[6] R. J. Wiener and D. F. McAlister, Phys. Rev. Lett. **69**, 2915 (1992).
[7] K. T. Coughlin and P. S. Marcus, J. Fluid Mech. **234**, 1 (1992).
[8] C. A. Jones, J. Fluid Mech. **157**, 135 (1985).
[9] G. Pfister, A. Lorenzen, and T. Mullin, Phys. Fluids **26**, 10 (1983).
[10] T. Mullin, Phys. Rev. A **31**, 1216 (1985).
[11] G. P. King and H. L. Swinney, Phys. Rev. A **27**, 1240 (1983).
[12] M. Gorman and H. L. Swinney, J. Fluid Mech. **117**, 123 (1982).
[13] L.-H. Zhang and H. L. Swinney, Phys. Rev. A **31**, 1006 (1985).
[14] K. T. Coughlin and P. S. Marcus, J. Fluid Mech. **234**, 19 (1992).
[15] J. von Stamm, Th. Buzug, and G. Pfister (unpublished).
[16] A. A. Predtechensky (private communication).
[17] G. Pfister and A. A. Predtechensky (unpublished).
[18] D. Coles, J. Fluid Mech. **21**, 3 (1964).
[19] G. Pfister and I. Rehberg, Phys. Lett. **83A**, 19 (1981).
[20] Y. Demay and G. Iooss, J. Mec. Theor. Appl. (France), Spec. Suppl. **193** (1984).
[21] G. Ahlers, D. S. Cannell, and M. A. Dominguez Lerma, Phys. Rev. Lett. **49**, 368 (1982).
[22] H. Brand and M. Cross, Phys. Rev. A **27**, 1237 (1983).
[23] M. Wu and C. D. Andereck, Phys. Rev. Lett. **67**, 1258 (1991).
[24] G. Pfister, U. Gerdts, F. Schulz, and G. Geister (unpublished). This paper is summed up in K. Bühler, J. E. R. Coney, M. Wimmer, and J. Zierep, Acta Mech. **62**, 47 (1986).
[25] T. Mullin, K. A. Cliffe, and G. Pfister, Phys. Rev. Lett. **58**, 2212 (1987).
[26] G. P. King, Y. Li, W. Lee, H. L. Swinney, and P. S. Marcus, J. Fluid Mech. **141**, 365 (1982).
[27] U. Gerdts, Ph.D. thesis, Universität Kiel, 1985.
[28] P. Fenstermacher, H. L. Swinney, and J. Gollub, J. Fluid Mech. **94**, 103 (1979).
[29] M. Gorman and H. L. Swinney, Phys. Rev. Lett. **17**, 1871 (1979).
[30] M. Gorman and H. L. Swinney, J. Fluid Mech. **117**, 123 (1982).
[31] A. Brandstäter, J. Swift, H. L. Swinney, A. Wolf, J. D. Farmer, E. Jen, and P. J. Crutchfield, Phys. Rev. Lett. **51**, 1442 (1983).
[32] J. von Stamm, Th. Buzug, and G. Pfister (unpublished).
[33] G. Pfister, K. Schätzel, and U. Gerdts, in *Laser Anemometry in Fluid Mechanics*, edited by D. F. G. Durao (Ladoan-Instituto Superior Técnico, Lisbon, 1984).
[34] R. Vehrenkamp, K. Schätzel, G. Pfister, B. S. Fedders, and E. O. Schulz-DuBois, Phys. Scr. **19**, 379 (1979).